Particle Image Velocimetry (PIV) measurements in a water film, application to a tire rolling through a puddle

Damien Cabut, Marc Michard, Serge Simoëns, Violaine Todoroff, Jean Lemaître, Correntin Hermange, Yohan Le Chenadec

Mechanics & Industry **20**, 811 (2019)
© D. Cabut et al., Published by EDP Sciences 2020
https://doi.org/10.1051/meca/2020052

Mechanics & Industry

Available online at:
www.mechanics-industry.org

Selected scientific topics in recent applied engineering – 20 Years of the 'French Association of Mechanics – AFM'

REGULAR ARTICLE

OPEN ACCESS

Particle Image Velocimetry (PIV) measurements in a water film, application to a tire rolling through a puddle

Damien Cabut[1,*], Marc Michard[1], Serge Simoens[1], Violaine Todoroff[2], Jean Lemaître[2], Correntin Hermange[2], and Yohan Le Chenadec[2]

[1] Université de Lyon, Ecole Centrale de Lyon and LMFA UMR CNRS 5509, 36 Avenue Guy de Collongue, 69134 Ecully, France
[2] Manufacture Française des Pneumatiques Michelin, Clermont-Ferrand, France

Received: 10 October 2019 / Accepted: 14 June 2020

Abstract. A measurement method based on Particle Image Velocimetry (PIV) with refraction of the laser sheet at a window/water interface is proposed for the measurement of the velocity field of a flow, inside a water puddle, due to a tire rolling on. This study focuses on the feasibility and repeatability of this optical measurement method. The characterization of the optical properties of this measurement technique defines its accuracy. The analysis of the overall features of the flow is focused on two main flow zones in front of and around the tire. The flow inside the first zone is characterized by a global velocity of the water displaced in an area located in front of the tire. In the second zone a velocity representative of the flow in the vicinity of the tire shoulder is also defined. Correlations of both characteristic velocities with the car speed and water film height are established. New and the corresponding worn tires were tested in this work.

Keywords: Free surface flow / tire / road contact / multiphase flow / particle image velocimetry

1 Introduction

The capacity of a tire to drain water, when rolling on a water puddle, is critical in order to avoid hydroplaning. This phenomenon happens when the water height and the vehicle speed are too high causing an accumulation of water in front of the tire. Due to this accumulation, the fluid exerts a lift force on the tire and, then, lifts the car up to the total loss of contact between the tire and the ground [1]. This causes a total loss of control of the vehicle. It has been demonstrated that current regulatory tests (on vehicle wet braking from 20 to 80 km/h on 1 mm water depth) have some hydroplaning phenomenon when worn tires are used [2]. This is why the design of the grooves of a tire has to be optimized in order to evacuate enough water to avoid hydroplaning. To be more specific, if the drainage effect is not sufficient, the effect of the tire load on the water in front of the contact patch area induces a high hydrodynamic pressure in proportion to the square of the vehicle speed [3].

Most experimental works related to hydroplaning are focused on the evolution of the contact patch area with different parameters as vehicle speed, water height or tire grooves geometry ([4–6]). The contact patch area identification is based on post-processing of images recorded with a camera below a window embedded on the road (were vehicle is moving and water puddle is present) and using fluorescent dye diluted in the water puddle [7] and a global illumination. The evolution of this contact patch area as a function of car speed is important in order to quantify the uplift of the tire due to the hydrodynamic pressure and in order to classify the tire groove patterns with respect to their efficiencies. However, those measurements do not allow to quantify water flow rate in specific regions, like in the water bank or inside the grooves. Such flow rate quantification requires the quantitative knowledge of the velocity field in the liquid film near the contact patch.

The state of the art related to the velocity field structure in the vicinity of the contact patch for a car rolling through a puddle and on a smooth ground is mainly concerned with numerical studies ([8–11]). On the other hand, to our knowledge, the literature related to velocity measurements is very sparse. The only available reference is the work done by Suzuki and Fukijama 2001 [12]. The authors performed measurements using a technique derived from the so-called particle tracking velocimetry (PTV). Velocity was deduced from the image recordings of the flow tracer particles (millet grain seeding) with a camera and a large exposure time of the camera. Those measurements provided a rough estimate of the water velocity direction at a large scale, of the order of the tire

* e-mail: damien.cabut@ec-lyon.fr

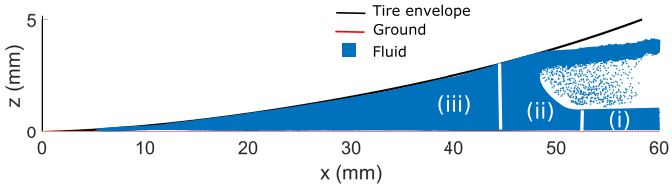

Fig. 1. Sketch of the different zones in front of the contact patch area.

width. The lack of seeding particles in the measurement domain didn't produce details at smaller scales. Furthermore the precision of velocity magnitude measurements was also limited due to the uncertainty in the length of the particle trajectories and the size of the seeding particles. Finally, measurements inside grooves were not available.

From the previous references, it is possible to summarize the main features of the flow structure in front of the moving tire as depicted in Figure 1. From the right to the left, three zones are identified:

i) a first zone where the fluid is at rest with a nearly uniform film thickness h_0. The free surface can locally be disturbed by the falling liquid entrained by the rotating tire and/or ejected above the free surface by the tire displacement;
ii) a second zone with a more complex three-dimensional structure, called the velocity front, where the fluid undergoes a sudden horizontal acceleration, up to a maximal velocity value. In this zone the streamwise velocity gradient generates locally large vertical velocity components combined with a local increase of the water film thickness, as well as a strong curvature of the film free surface until the contact line with the tire surface. Moreover some splashes can be generated above the free surface in front of the tire and break-up into a non-continuous liquid phase including filaments and/or droplets falling on the free surface of region i);
iii) a third zone confined in a region located between the velocity front and the contact patch area, where the flow structure recovers a more simple structure: both ground and tire surfaces prevent the appearance of large vertical velocities due to flow confinement between these two solid boundaries. In the central part (transversally) of the tire, the fluid is pushed by the tire mainly in the streamwise motion. In regions located around the shoulders of the tire, this streamwise motion is combined with large spanwise velocities generated by the geometric blockage effect of the tire. The remaining liquid is trapped downstream inside grooves.

The balance between the amount of liquid pushed in front of the tire, flowing around the shoulder and trapped inside grooves is a complex function of different operating parameters, like the water thickness h_0, the car velocity V_0 and the tire geometric characteristics.

In the present work, the influence of these parameters on measurements is explored inside the third zone iii) located in front of the tire, including the shoulder zone; the flow inside grooves is not of the scope of the paper.

Measurements are performed using a technique derived from the so-called Particle Image Velocimetry (PIV). PIV is an extensively used method in fluid mechanics for the measurement of instantaneous velocity fields [13,14]. Seeding particles introduced in the fluid are illuminated with a double pulsed laser light sheet. A pair of particle images is recorded with a double frame camera and processed using a cross-correlation algorithm to determine the displacement of particle patterns in the flow; displacements are converted into velocity components knowing the time delay between laser pulses. To our knowledge, this method has never been used for measurements in the liquid phase displaced by a real tire rolling through a puddle.

The measurement method and test facility are detailed in Section 2 with description of optical parameters of the measurement method. Then the tire model and the different zones of study are presented. Measurement results are given in Section 3; the characteristic of seeding spatial distribution is used for image processing. A double spatial and ensemble averaging process is described in order to analyse the influence of operating parameters on some characteristic fluid velocities in front of the central rib and around the shoulder of the tire. Finally perspectives and conclusions are discussed in Section 4.

2 Experimental facility and methods

2.1 Facility and set-up

In this work, measurements are performed on a dedicated track at Michelin© Ladoux site (France)©. This track is composed of a straight road portion on which is superimposed a water film containing seeding particles as depicted in Figure 2. The thickness h_0 of the water film, when fluid is at rest, is regulated with an ultrasound probe which controls the opening of valves at the inlet and outlet of the puddle. Due to safety considerations, both emitting and receiving optics for the present visualisation technique, cannot be placed at the ground level, neither in front of the tire, nor on the side of the water puddle. Therefore, seeding particles cannot be illuminated by a light sheet parallel to the ground as should be done for a classical PIV measurement arrangement. To overcome this constraint, a PMMA transparent window whose thickness is 500 mm is embedded in the ground and provides an optical path from a room below the road. The originality of the present set-up is based on the refraction of the illumination light sheet at the PMMA/water interface, as shown in Figure 2. Details of this specific optical arrangement are described in the next section.

2.2 Emitting and receiving optics characteristics

2.2.1 Emission

The laser sheet is generated by a double cavity pulsed $Nd:Yag$ Laser (Litron Bernoulli) emitting at a wavelength of 532 nm. The energy of each pulse is around 100 mJ and their length around 5 ns. The light is generated using sheet optics composed of a spherical divergent

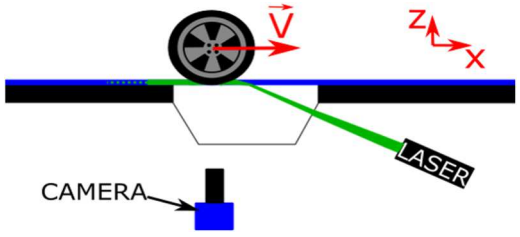

Fig. 2. Scheme of the illumination method.

lens in order to enlarge the laser beam before a convergent lens which minimizes the thickness of the laser sheet at the beam waist. A cylindrical divergent lens spreads the laser beam in the spanwise direction (compared to axis beam direction). The light sheet optics are placed on a rotation stage to select the proper incident angle of the incoming laser sheet on the PMMA prism. In order to obtain a laser sheet propagating inside the water film with the lowest as possible inclination angle (compared to the horizontal road), the window has a prismatic shape with an inclined side. The angle between the upper horizontal face (road level) and the inclined face is equal to $\theta_p = 66°$. This value of θ_p is close to the critical angle ($\theta_c = 63.2°$) of total light reflection at a $PMMA/water$ interface with respect to standard Snell-Descartes laws:

$$\theta_t = a\sin\left(\frac{n_p}{n_w}\sin(\theta_i)\right) \quad (1)$$

$$T = 1 - R = 1 - \left|\frac{\tan\left(a\sin\left(\frac{n_p}{n_w}\sin(\theta_i)\right) - \theta_i\right)}{\tan\left(a\sin\left(\frac{n_p}{n_w}\sin(\theta_i)\right) + \theta_i\right)}\right|^2 \quad (2)$$

where $n_p = 1.49$ and $n_w = 1.33$ are respectively the theoretical refractive indices of water and PMMA transmission media, θ_i is the incident ray angle before the interface, θ_t is the transmitted ray angle, T is the transmission coefficient between PMMA and water and R is the reflection coefficient at the interface.

The precision on this angle is approximately equal to 0.1°. The orientation angle of the laser sheet optic has to be taken with a slight offset of approximately $5° \pm 0.5°$ compared to the normal of the inclined face of the prism to obtain enough transmission T of the light sheet to illuminate particles. In this configuration, the transmitted angle in the water puddle, according to equation (2) is approximately $\theta_t = [77°; 80°]$ to the normal of the interface.

2.2.2 Seeding

With this refracted illumination method, the main optical noise sources collected by the camera are

i) spurious light trapped in the prism due to the part of the beam reflected at the interface which propagates inside the PMMA with secondary reflections on the tire and
ii) ambient light above the water film.

This noise can be reduced by the use of fluorescent particles and camera filter. The chosen particles emit light at a higher wavelength than the illumination laser light. Therefore, by selecting the wavelength of the emitting particles with an adequate reception filter, spurious light is strongly reduced to ensure a good signal/noise ratio. The wavelength of the light emitted by fluorescence is around 584 nm. The diameter of fluorescent particles lies in the range 20−50 µm. The mean diameter is about 35 µm. Note that temperature is variable ($T = 6°$C to $T = 12°$C) due to night trials. Particles are more ovoïdal than spherical one.

Table 1. Time delay between laser pulses.

Vehicle speed V (km/h)	30	40	50	60	70	80
Time step δt (µs)	330	225	180	150	130	115

2.2.3 Reception

Images of fluorescent particles are recorded with a double frame sCMOS camera whose optical axis is perpendicular to the lower horizontal face of the PMMA window. The camera is placed below the prism (Fig. 2).[1] The camera sensor size in the streamwise and spanwise directions are respectively 2560 pixels and 2160 pixels.

An optical filter with a band-pass width of 20 nm and centred at 590 nm is used for filtering all wavelengths out of interest. The efficiency of this filter is quantified by the transmission of 93% inside the band-pass window and 3% outside. The size of the measurement area (AI) is determined by a magnification factor M equal approximately to 0.01. The factor M depends on both focal distance, equal to 100 mm, an aperture fixed to 5.6 and on the working distance between lens and water film, nearly equal to 1150 mm. The size of the camera field of view is around 245 mm in the streamwise direction and 205 mm in the spanwise direction. This size is defined in order to capture the flow over a spanwise length scale which is nearly equal to the tire width. The time delay between laser pulses depends on the vehicle speed according to Table 1. With a 75% overlapping factor, the final size of the interrogation areas used in the iterative process for the cross-correlation between images is 32×32 pixels^2. In other terms the physical size of the final AI is 3.05×3.05 mm^2.

2.2.4 Laser and camera synchronization

Synchronization between laser pulses and image recording is performed using a commercial software (Davis) and a programmable timing unit (PTU) synchronising laser and camera. Optical sensors, located along the track some meters upstream the water puddle, measure the actual car velocity before car arrival inside the water puddle zone. A trigger signal is then generated and sent to the PTU, using a real-time dedicated processor, with a time delay after the arrival in front of the last optical sensor. This time delay is adjusted in order to start and synchronize both laser firing and camera opening sequences when the tire is located at a chosen streamwise position above the transparent window, inside the camera field of view. The frequency of

[1] This measurement method is patented (patent n° FR1900180).

Table 2. Number of passes for ensemble averaging.

Tire type	30 km/h	40 km/h	50 km/h	60 km/h	70 km/h	80 km/h
New tire	20	8	16	20	16	2
Worn tire	28	28	28	28	28	8

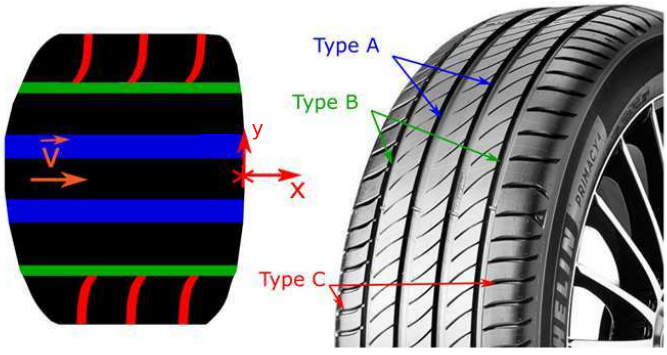

Fig. 3. Scheme of the contact patch area of a PCY4 tire. Red are the Type C grooves, green are the Type B grooves and blue are the type A grooves.

both pulsed laser and camera are not high enough to perform time resolved measurements. Therefore, a single shot measurement is performed for each run by recording an image pair. The overall measurement process is repeated over several runs without changing the operating parameters in order to perform some statistical analysis. After each run, some water is projected outside the water bank, and the water height has decreased. A time delay is necessary for the hydraulic loop to stabilize the water height at the initially specified value. The number of independent statistical samples are summarized in Table 2.

2.2.5 Tire model, coordinate system and operating parameters

The tire used in this study is a commercial summer tire with specifications $225/45R17$. This tire is composed of two large longitudinal grooves, two thinner longitudinal grooves and transverse grooves as depicted in Figure 3. For all the following measurements and results, the inflation pressure of the tire is set to 2.2 bars. The coordinate system shown in Figure 3 is defined by an horizontal axis x parallel to the car motion, a spanwise horizontal axis y and a vertical axis z. Due to the fluctuating position of the tire inside the field of view from one trial to the other, the origin of the coordinate system needs to be defined by identifying the contact patch position for every measurement in both x and y directions, according to a special procedure described in Section 3.1. The vertical origin of the coordinate system is always fixed at the ground level, i.e. at the $PMMA/water$ interface. The car velocity V_0 is varying in a range between 8.33 m.s^{-1} and 22.2 m.s^{-1}. The water film (initial water puddle) thickness h_0 is specified to a value ranging from 1.5 mm for worn tires up to 8 mm for new tires. The value of h_0 is regulated thanks to an ultrasound probe which controls, in real-time, the flowrate inside a closed-loop water circulation device using a pump and vanes located below the track.

2.3 Illumination and depth of focus

For image analysis , Particle Tracking Velocimetry (PTV) is based on the identification of individual particles, and becomes inefficient if particle density is too high. On the other hand, PIV analysis is based on the computation of cross-correlation between particle images in both frames of an image pair. This cross-correlation is performed between elementary interrogation windows containing a set of seeding particles. The main parameter influencing the measurement of the cross-correlation peak is the intensity of particle images on the camera sensor I_i (as expressed by R.J Adrian et al. 1991 [14]):

$$R_D = \sum_{x=0,y=0}^{x<n,y<n} I_1(x,y) \cdot I_2(x+\mathrm{d}x, y+\mathrm{d}y) \qquad (3)$$

where R_D is the displacement component of the cross correlation function, x and y are the streamwise and spanwise coordinates inside the elementary interrogation window, n is the size of the interrogation window, $(\mathrm{d}x, \mathrm{d}y)$ are the displacement components inside the interrogation window taken in the first and the second images and I_1 and I_2 are the intensities of the images 1 and 2 respectively.

For each interrogation area, the location $(\delta x, \delta y)$ in the correlation plane of the peak value of R_D determines the particle displacement components related to the most probable displacement of particles inside the interrogation window. The velocity components in this area are finally derived by dividing δx and δy by δt, the time separation between single shot pulses. The velocity measured with the PIV technique is then directly related to the intensity of particle images. This intensity is a combination of two optical parameters which are:

i) the illumination of the particles and
ii) the position of the fluorescent particles in the depth of view (due to the depth of focus) of the camera. Therefore in order to identify particles in the water volume which contribute more in the signal for velocity determination, the depth of view and the illumination function of the particles at different heights in the puddle have to be determined.

Specific measurement methods are used in-situ when water is at rest to quantify the depth of field and the particle illumination profile at different height in the puddle. Firstly, the depth of view is measured using a dotted matrix, composed of black dots of diameter 0.125 mm with a 0.250 mm space between them, dots disposed on a white plate (Fig. 4b). The matrix is parallel to the window

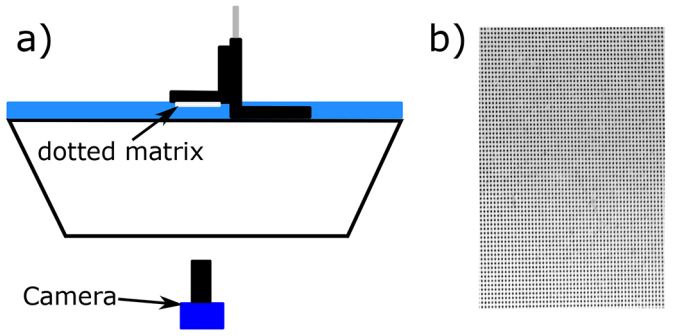

Fig. 4. a) Scheme of the dotted matrix on the translation stage in the puddle with the camera below the PMMA block. b) Image of the dotted matrix.

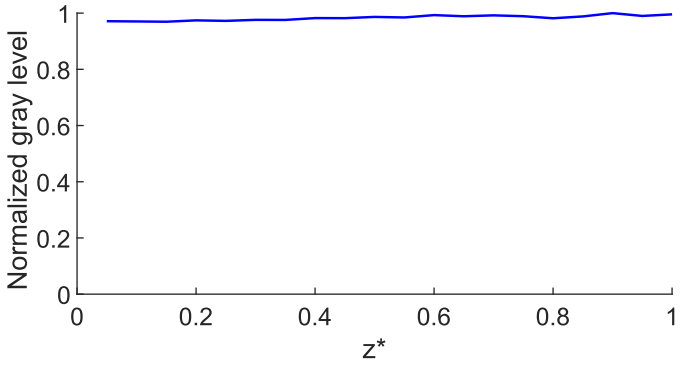

Fig. 5. Gray level of dots function of the normalized height ($z^* = z/h_0$) for a working distance of 1150 mm between the camera and the PMMA block.

(road level) and vertically located using a vertical translation stage with a precision of 0.01 mm. Some images of dots are recorded at every location for a distance between ground and dotted matrix varying in the range 0.2 mm to 4 mm with a step of 0.2 mm (Fig. 4a).

The depth of field is based on the analysis of dot gray-level images. When dots are out of focus their apparent diameter increase while their intensity decrease. Therefore, the inverse of dot intensity ($1/I_{\text{dots}}$) gives an information on the darkness of the dots and their quality of focus. This parameter is averaged on approximately 3500 dot images from the matrix and for every altitude of the matrix that gives a gray-level $GL(z^*) = \text{mean}(1/I_{\text{dots}})$ ($z^* = z/h_0$). A normalization of this gray-level is made as $NGL(z^*) = GL(z^*)/\max(GL)$ Fig. 5).

The depth of focus of the receiving optic is directly linked to the distance between the lens and the measurement zone [15]. Therefore these specific In-situ measurements are made for the working distance used for trial PIV measurements. The grey-levels in the height of the puddle does not vary significantly in the whole water height. This shows that the focusing of particles is the same in all the puddle for the camera position and aperture used during all our trials. Therefore, particle focus does not influence the cross-correlation calculation.

To determine the light sheet longitudinal intensity profile, an inclined fluorescent plate (Fig. 6) is placed in the puddle at different longitudinal locations x in the

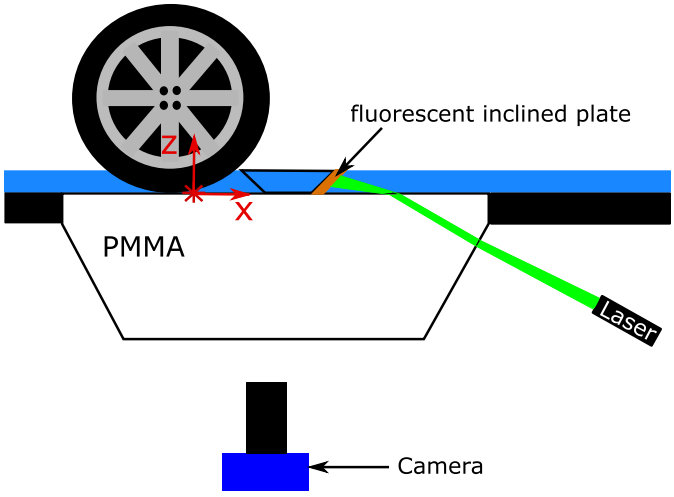

Fig. 6. Scheme of the inclined plane in the puddle.

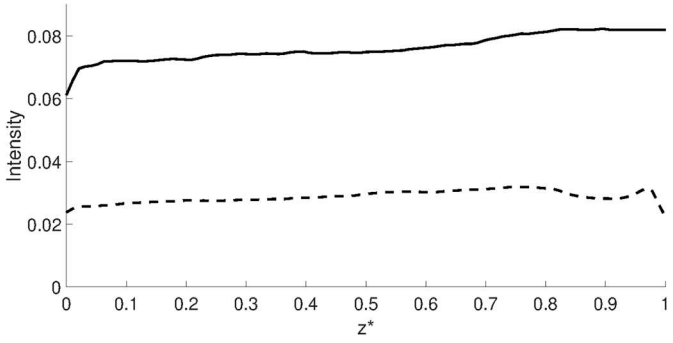

Fig. 7. Intensity function of the normalized height in the puddle ($z^* = z/h_0$), line for the location 1 and dashed line for the location 2.

measurement area. The sheet of light hit the plate at an height z^*. The fluorescent light re-emitted from the inclined plate is recorded with the camera (disposed as it is during trials). The average intensity in the spanwise plate direction y is then plotted to know the light sheet intensity profile at a given height z^* of the puddle.

The inclined plate is thus placed at 2 different x locations which are located based on the coordinate system presented in Figure 6 with the origin at the centre of the contact patch area in the spanwise direction and at the beginning of the contact patch area in the streamwise direction. The chosen measurement locations are one, before the tire contact patch area, at $x = -140$ mm and second (at a distance of approximately $d = 300$ mm from the laser sheet emergence in water), at the beginning of the tire groove, at $x = 12.5$ mm (at a distance of approximately $d = 450$ mm from the laser sheet emergence in water). The measurements show that the intensity profile is almost uniformly constant in the height for every x location in the measurement area (Fig. 7). This result can be qualitatively explained as follows. The laser sheet emerging from the transparent window just after refraction is propagated inside the liquid film with an angle nearly equal to 10°. After some travel distance, the light sheet has multiple reflections at the free surface and the

intensity profile spreading is sufficient to produce a nearly uniform profile. The chosen angle induces a laser sheet propagation angle of around 10° compare to the horizontal interface (which correspond to the transmitted angle θ_t calculated in Sect. 2.1) in the water because of the strong loss of energy at the interface when the angle is low. In order to have enough signal, T (Eq. (2)) have to be large enough to transmit light in the water, then θ_t could become larger. Therefore, the illumination of particles is considered as homogeneous in the volume of interest.

With those optical parameters, all particles in the puddle are illuminated with the same intensity and well focused at every locations. every particle image in the measurement volume contributes with the same weight to the cross-correlation algorithm. However, this cross-correlation function is a summation of all particles' contribution. Therefore, the particle density per unit of height is also important in the calculation and is considered as homogeneous as a first approximation.

We have now to focus on the behaviour of the seeding particles that is a second key point of the measurement technique. Contrarily to illumination we use classical seeding particles for large field of view. The previous described illumination allows for such particles to re-emit enough light to be recorded on the sCMOS camera.

2.4 Motion of seeding particles

For safety considerations and in order to maximize the ratio between light intensity from fluorescent particles and spurious light intensity, measurements are made during the night. Seeding particles are first introduced in the puddle and mixed with water in the measurement region. Then, the car driver starts the car rolling to the puddle. To control the speed of the car, the speed controller is activated. The overall time between the seeding of the puddle and the triggering of the PIV is around 30 s. During this time a first bias could be due to the sedimentation of seeding particles falling in the water puddle. To quantify this effect in the following is considered a simplified equation of the particle falling in a steady puddle, taking into account the gravity, the buoyancy and the Stokes forces:

$$\frac{d\vec{V_p}}{dt} = \frac{\rho_p - \rho}{\rho_p}\vec{g} - \frac{18\mu}{\rho_p {d_p}^2}\vec{V_p} \tag{4}$$

$$\Rightarrow V_p(t) = -\tau_p \frac{\rho_p - \rho}{\rho_p} g \left[1 - e^{-t/\tau_p}\right] \tag{5}$$

where $\tau_p = \frac{\rho_p {d_p}^2}{18\mu}$ is the characteristic falling time, where ρ_p is the particle density, d_p is the particle diameter and μ is the fluid viscosity.

With the time integration of the falling velocity (Eq. (5)) (from 1 10^{-5} m.s^{-1} to 2.7 10^{-5} m.s^{-1} for the present particles), the vertical distance travelled by a particle (z_f), between the mixing of seeding particles in the puddle and the car passing in the AI, can be calculated. This distance travelled by the smallest ($d_p = 20$ µm) and the largest ($d_p = 50$ µm) fluorescent particles during these 30 s are respectively $z_f = 0.8$ mm and $z_f = 5.2$ mm. The initial seeding is considered as homogeneous. Therefore, with this protocol, the falling velocity could induce an higher density of particles at the lowest altitudes, which contributes the most to the cross-correlation. Therefore, the velocity measurements could tend to privilege the velocity in the lowest part of the film. Nevertheless it has to be noted that a large part (30%) of the particles are in the range 30 µm to 40 µm and that their shape is spherical. Thus from such falling velocity we have the worst trend.

Another bias could be the ability of the seeding particles to follow the fluid movement during an acceleration phase. The most important acceleration of the fluid in this problem occurs inside the front velocity (ii) in Figure 1. To quantify this capacity to follow the fluid movement, the Stokes number is calculated comparing the relaxation time of the particle $\tau_p = \frac{\rho_p . d_p^2}{18.\mu}$ (given above for the chosen particles) and a characteristic time of the flow $\tau_c = \frac{\delta}{U_{\max}}$ (where $U_{\max}$ is the maximum velocity in the water bank (around 22 m.s^{-1} for the highest car velocities, given a characteristic time about 3.6 10^{-4} s) and δ is the water height (it is around 8 mm). The Stokes number ranges from $\frac{\tau_p}{\tau_c} = 0.04$ to 0.25 for particles from the smallest to the largest. This can still be considered as a good flow tracer for the smallest ones but it is at the limit for the largest (compare to $St = 0.1$ that could be considered as the limit of a good tracer behaviour). These estimations are coarse as shape and four way coupling is not accounting here. Nevertheless for the present experiments as we have a large field of view we have chosen to keep these particles (from a light re-emission point of view) as it is usual for large field of view. Nevertheless in the trial situations even the largest worst seeding particles have a behaviour good enough for our PIV analysis of our flow. Note that calculation was done with the highest car speed and that with the lower car speed behaviour also improved.

3 Measurements and results

The objective of the present section is to estimate characteristic fluid velocities inside different zones of interest located in front of the tire. The first zone of interest is located upstream the front edge of the contact patch area, near the central rib tire. In this part the water is pushed along the tire rolling direction. The second flow area of interest is located near the shoulder where large spanwise velocities are generated. This part of the flow determines the amount of water that gets around the tire and which is not drained by the grooves.

We focus here on the evolution of these characteristic velocities as a function of our operating conditions: the car speed, the water height or type of tire (*new*/*worn*).

3.1 Location of the contact patch area: definition of a common coordinate system

Examples of the first frame of an image pair recorded for $V_0 = 17.5$ m.s^{-1} are given in Figure 8 with two independent snapshots. These images highlight two major

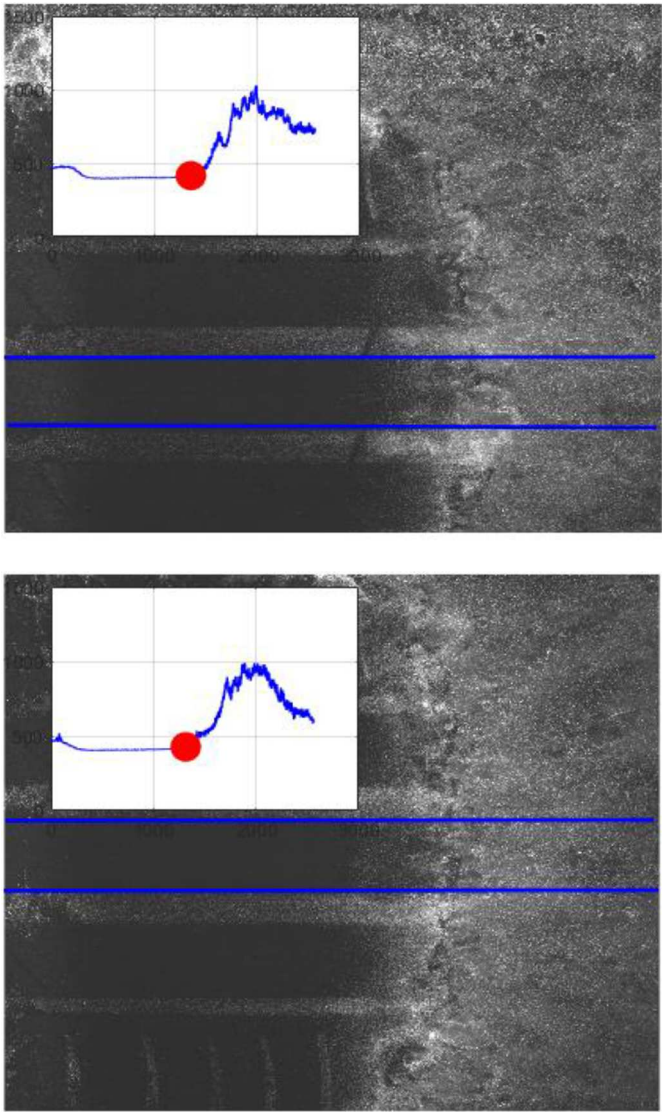

Fig. 8. Raw images and spatially averaged grey level along the central ribs; the location of the front edge of the contact patch is shown by the points.

necessity of the images to be processed for every run before PIV analysis:

– the spanwise and (or) the streamwise shifts of the tire location inside the field of view.
– the spatial variability of the grey-level images, mainly due to inhomogeneties of the seeding particle dispersion inside water.

For both images, the spanwise location of the tire is easily identified by examining the modulation of the grey-levels along a transverse line passing through the longitudinal grooves. On the other hand, it is harder to determine the streamwise location of the tire inside the field of view as the limits of the longitudinal contact patch area are less neat. Moreover, even if the spatial jitter of the streamwise geometric location of the tire is exactly zero (an exact patch area determination), the flow can locally present some variability from one snapshot to the other for, at least two reasons:

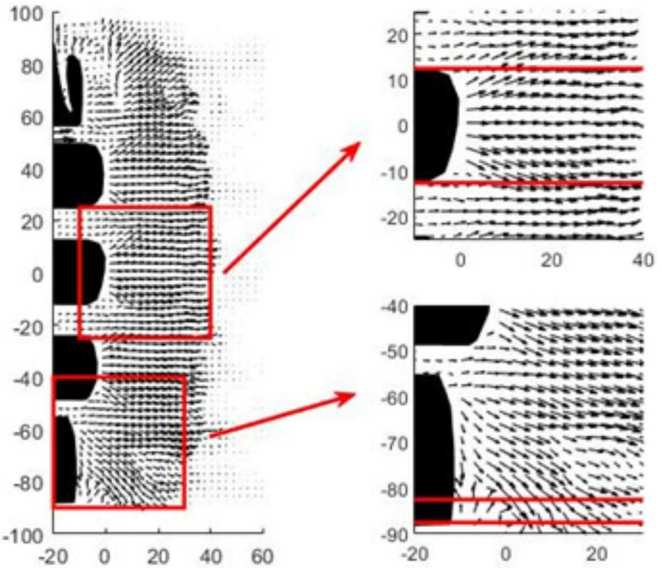

Fig. 9. y-Spatial averaging of $U_y(x,y)$ and $U_x(x,y)$ (vectors are $(U_y(x,y), U_x(x,y))$) inside the narrow bands limited by lines.

i) the local seeding particle density can undergo some variability;
ii) the local velocity field near the shoulder can undergo a variability related to the random transverse grooves location inside the field of view.

Therefore, we define for each snapshot the origin of the coordinate system as the location of the front edge of the contact patch area near the central rib as follows. The evolution of the grey-level along the horizontal direction (x) inside the two previous images is given in Figure 8; this profile is obtained by spatially averaging the local grey-levels over a narrow band (delimited by blue lines in both images of the figure). The band width is equal to the geometric width w of the central rib. It appears that this averaged profile is nearly uniform along the central rib and has a sudden increase and a peak in front of the rib. We arbitrary define the axial position x_c of the front edge of the contact patch area as the point where the grey-level exceeds, e.g., 5% of the nearly uniform grey-level along the central rib. The spanwise location y_c of the front edge is defined as half the distance between the central rib longitudinal edges. The resulting location of the coordinate system origin is given as shown by red points in Figure 8. The standard deviation values of x_c an y_c are respectively around 5 mm and 15 mm for the worn tire.

3.2 Variability of velocity measurements

The variability of the velocity field localisation has been previously minimised as shown in the previous section. Nevertheless, the velocity field can show some disparity from one measurement to the other as shown in Figure 9 for an instantaneous velocity map obtained for $V_0 = 17.5\,\mathrm{m.s^{-1}}$. The variability is visible near the shoulder and in front of the longitudinal grooves (shown with squares in the left part of the figure). Near the shoulder (down zone) the variability could be explained according

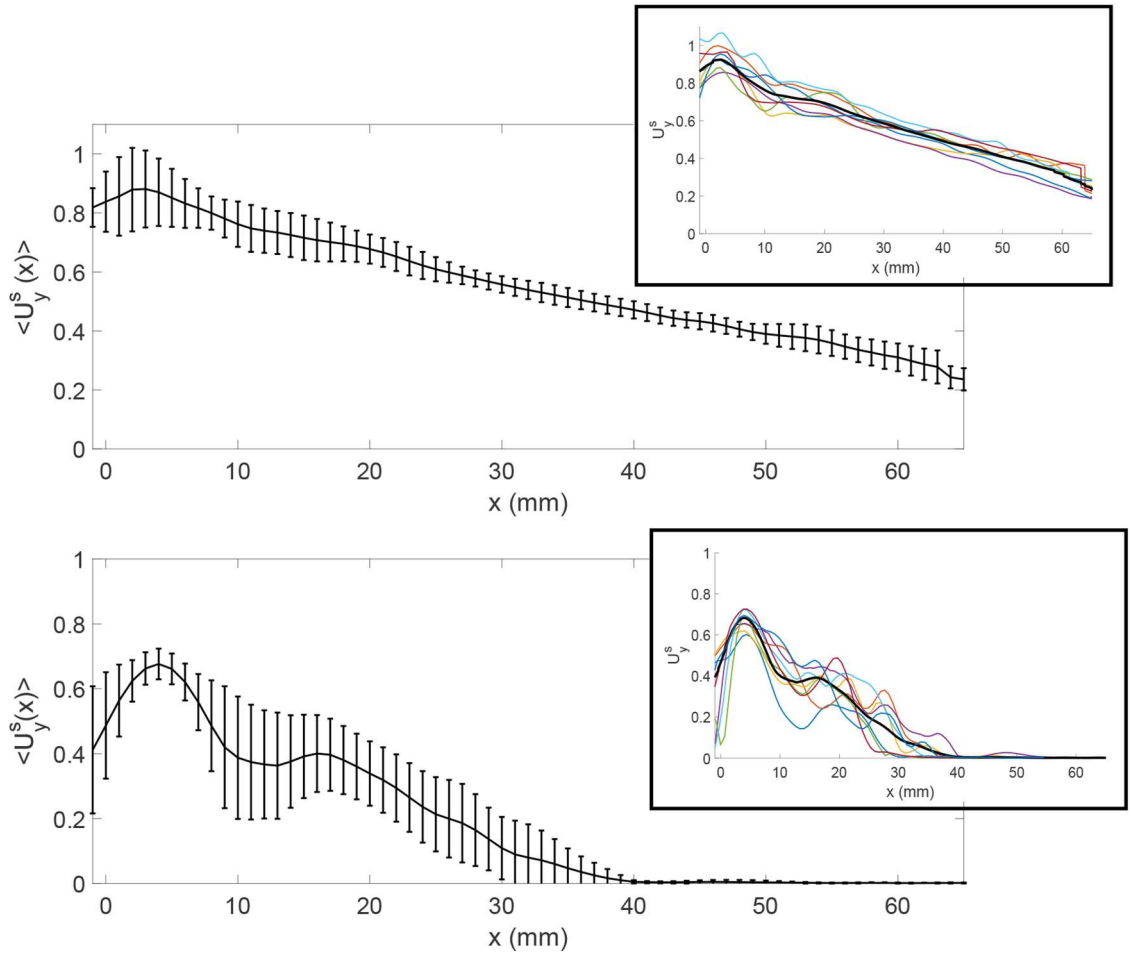

Fig. 10. Example of ensemble averaged velocity profile $\langle U_y^s(x)\rangle$ and the associated variability bars deduced from the instantaneous velocity profiles $U_y^s(x)$ shown on the upper right corner for new (up) and worn (down) tires. All is non dimentionalised by the tire velocity V_0.

to the random position of the transverse grooves near the edges of the contact patch area. For the front location (up zone) it is less clear at the present stage due to complex 3D two phase flow. In order to define characteristic velocities in front of the central (resp. near the shoulder) zone, we first perform a spatial averaging along y of velocity profiles $U_x^b(x,y)$ (resp. $U_y^s(x,y)$) in the two narrow bands limited by the red lines as shown on the right part of Figure 9. As an example the resulting profiles $U_y^s(x)$ (no more dependence on y), non dimensionalised by V_0, at the shoulder are shown in Figure 10 up and down for $V_0 = 17.5$ m.s^{-1} and respectively for a new and a worn tire.

It can be seen that for a new tire, despite some local differences, the overall feature of the profiles is identical from a snapshot to the other: a peak is measured near the tire, and the velocity is decreasing linearly with x in front of the shoulder. On the other hand, the situation is quite different for a worn tire: even if the velocity profiles can be superimposed around their main peak value, the remaining part of the profiles fluctuate from a shot to the other and even presents a secondary peak. The overall feature of the profile is not linear. The large variability of these profiles can be explained by the fact that the velocity measurement for worn tire and small values of the water film height h_0 is highly more influenced by the random location of the transverse grooves. Local perturbations of the flow in front of and around the shoulder are related to the flows inside transverse grooves.

3.3 Characteristic velocities in the water bank and at the shoulder

For the shoulder and every case, we derive, from the set of velocities profiles as those shown in Figure 10 (left upper square), global characteristic velocities, denoted $\langle \max.U_y^s\rangle$ and $\langle \max.U_x^b\rangle$, defined as the ensemble average value performed over the peak value of every profile $U_y^s(x)$ and $U_x^b(y)$ respectively.

Having in mind the physical significance of the flowrate due to the spanwise motion of water around the shoulder, we also define a more global characteristic velocity U_d^s, integrating the profiles from the tire until the last point of the shoulder zone: $U_d^s(x) = (\frac{1}{L}).\int_0^L U_y^s(x,y).dx$, with L the length of the shoulder line. For the new tire L is 100 mm and for the worn tire L is 40 mm. Such quantity

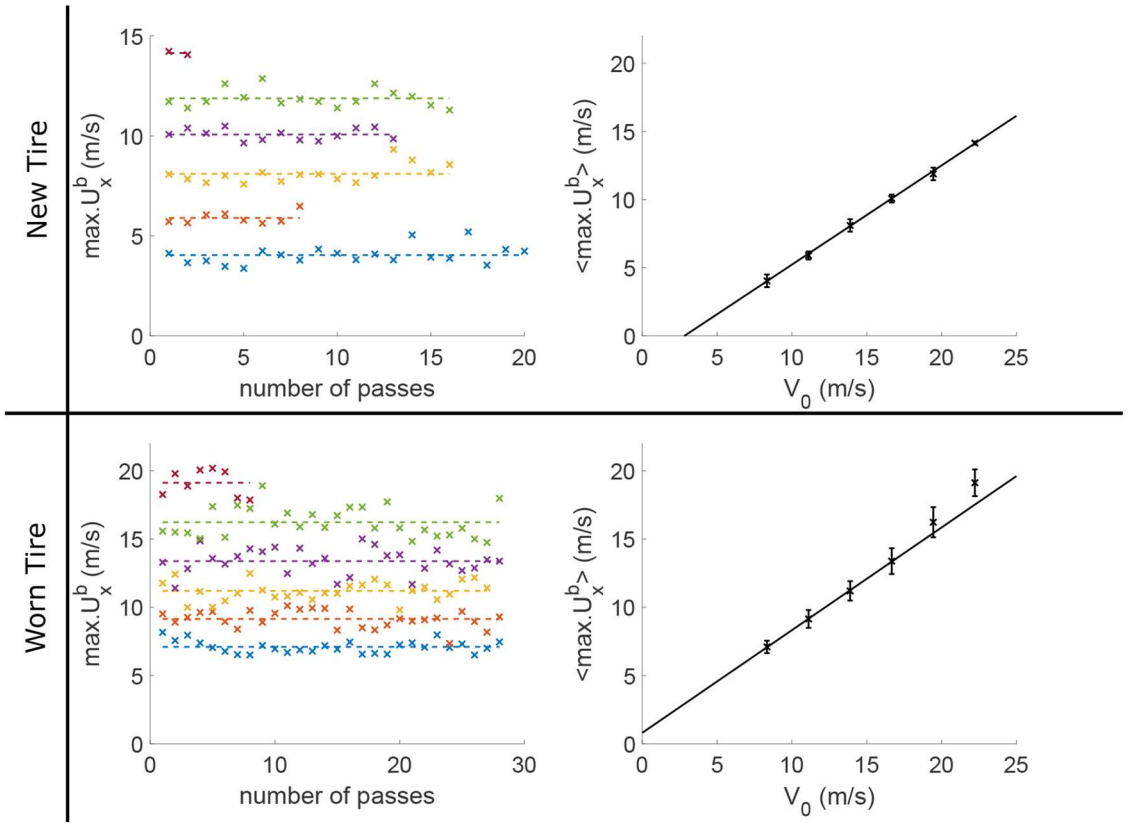

Fig. 11. On the left, max.U_x^b characteristic velocity in the water bank for every runs (crosses) for all vehicle speeds for new (up) and worn (down) tires (blue $V_0 = 30$ km/h, orange $V_0 = 40$ km/h, yellow $V_0 = 50$ km/h, violet $V_0 = 60$ km/h, green $V_0 = 70$ km/h and red $V_0 = 80$ km/h). The dashed lines represent the mean value deduced from all runs. On the rigth is the ensemble averaged value $\langle \text{max.}U_x^b \rangle$ obtained from the left values. solid lines are linear regressions for both cases (up and down). Error bars are associated errors deduced from the used runs (left).

could be considered as a flowrate, the water height being hypothesised constant.

The evolutions of $\langle \text{max.}U_x^b \rangle$ as a function of V_0 is shown in Figure 11 and the ones of $\langle \text{max.}U_y^s \rangle$ and $\langle U_d^s \rangle$ as a function of V_0 are shown in Figure 12 for the new (up) and the worn (down) tire. For a new tire, both characteristic velocities vary linearly in the range of variation of the car speed. For a worn tire, the evolutions are linear in a more limited range of V_0 values, and a small departure from linearity is observed for the highest car speeds.

3.4 Hypothesis on the linearity

In those studies, it appears that both velocities (streamwise in the water bank and spanwise at the shoulder) evolve linearly as a function of the car speed depending on the tire wear and the water height.

This linearity regarding the evolution of the speed and for the velocity in the water bank, $U_x^b(V_0)$, can be explained by the fact that the water which is not drained is pushed out by the tire in front of it. This linearity depends on the different parts of the flow. In a first approximation, in the tire referential, if a 2D flow is considered, the conservation of the mass flow rate in front of the tire gives a linear dependence between V_0 and every variable U^b and U_{grooves}, the average draining velocity in the grooves. Therefore, a disturbance in the linear evolution in one of these variables introduces a similar effect on other variables. The deviation from the linearity progressively appears with the highest car velocities. The same reasoning could be applied to the shoulder zone (Fig. 12). Due to its definition the equivalent flowrate velocity U_d^s has the same linear behaviour but in a lower velocity range. At the highest car speed the linear behaviour disappears. Only the new tire at the water bank zone could be considered to continue a linear trend. From a statistical point of view there is a maximum of 30 samples to obtain a given point in the right part of these plots. This is thus difficult to conclude as dispersion shown by the error bars are sufficient to invalidate any explanation. It has to be noticed that a certain number of uncertainties exist concerning few parameter of the present runs. This is out of the scope of this paper. But it is also acceptable to propose a rolling process modification in this zone. This will be interesting to have deeper studies to clarify this point.

4 Summary and conclusions

In this study we show that using a measurement method based on the refraction illumination and PIV, it is possible to quantify the velocity field in the puddle water flow

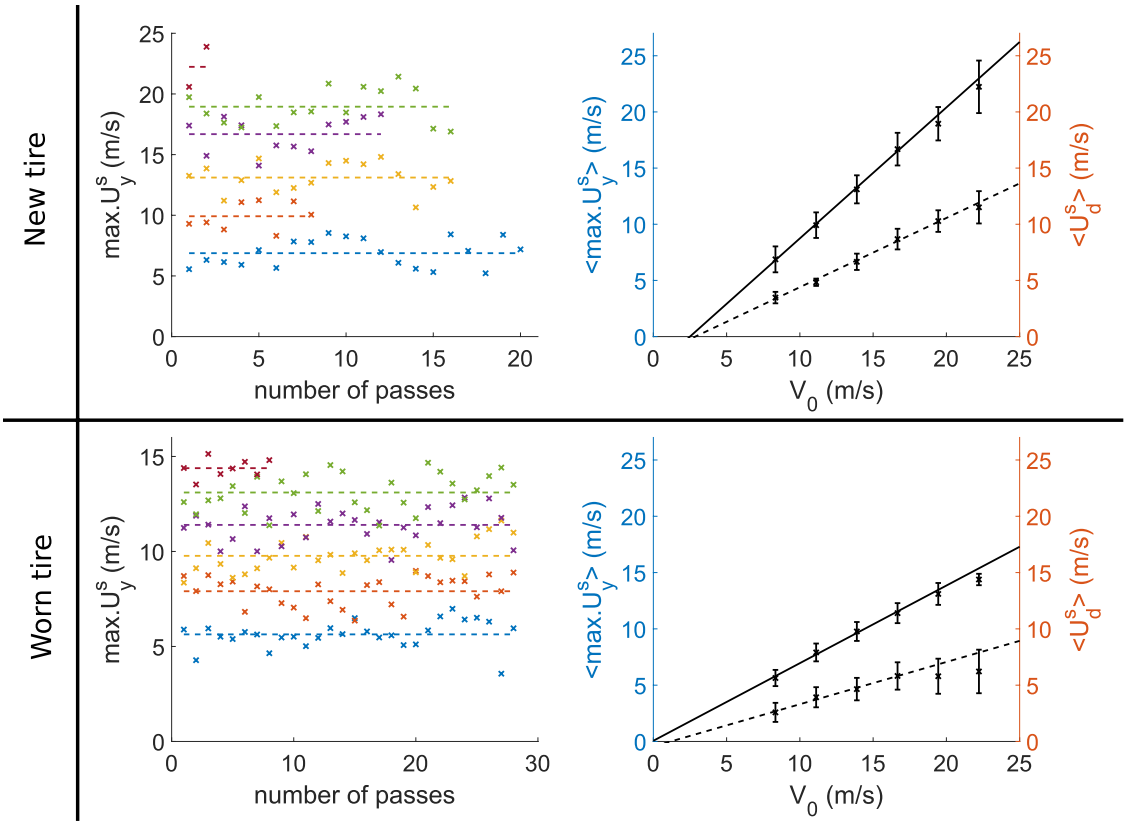

Fig. 12. On the left, max.U_y^s characteristic velocity in the shoulder for every runs (crosses) for all vehicle speeds for new (up) and worn (down) tires (blue $V_0 = 30$ km/h, orange $V_0 = 40$ km/h, yellow $V_0 = 50$ km/h, violet $V_0 = 60$ km/h, green $V_0 = 70$ km/h and red $V_0 = 80$ km/h). The dashed lines represent the mean value deduced from all runs. On the right solid line is the ensemble averaged value $\langle \text{max}.U_y^s \rangle$ obtained from the left values. Dashed line is the quantity U_d^s. Solid lines are linear regressions for both cases (up and down). Error bars are associated errors deduced from the used runs (left).

Table 3. Table of the standard deviation in max.U_x^b in percentage of the vehicle speed.

Case	30 km/h	40 km/h	50 km/h	60 km/h	70 km/h	80 km/h
PCY4 New	5.6%	2.7%	4.1%	1.8%	2.4%	0.5%
PCY4 worn	5.5%	5.9%	5.1%	5.7%	5.4%	4.4%

Table 4. Table of the standard deviation in max.U_y^s in percentage of the vehicle speed.

Case	30 km/h	40 km/h	50 km/h	60 km/h	70 km/h	80 km/h
PCY4 New	13.8%	10.3%	9.0%	8.5%	7.7%	10.5%
PCY4 worn	7.2%	7.1%	6.1%	5.4%	5.0%	2.5%

when a car is rolling through. The number of trials and the obtained results allow to conclude on a statistical behaviour. The low error bar levels, obtained from the associated standard deviation (presented in Tabs. 3 and 4), is satisfying and various trails exist to decrease it.

In this work, two areas of interest (AI) have been analysed in order to draw the main scheme of this 3D complex flow that even could involve in some parts two phase flow processes. In these AI, a main trend is described, the evolution of characteristic velocity is directly related to the vehicle speed. This evolution can be considered as linear depending on the tire wear and the water height. The streamwise characteristic velocity evolution in the water bank and the spanwise characteristic velocity at the shoulder are deduced from linear regressions until an inflection at a critical speed level. This critical speed indicates a change of regime and is approximately equal to 60 km/h for the worn tire with a water film depth $h_0 = 1.5$ mm and seems beyond 80 km/h for the new tire with $h_0 = 8$ mm (Fig. 12). To determine clearly if the inflection point exists (and if it is not an artefact) for the new tire and what is more precisely its value, new measurements have to be done for obtaining a greater number of points at the $V_0 = 80$ km/h case and to acquire points at $V_0 = 90$ km/h.

To improve the flow analysis, parametric studies can be carried out in order to determine the linear relationship coefficients and the critical velocities as a function of the

water film height, the wear of the tire and the tire pattern dimensions and drawings (if they are not artefact).

The present used measurement method allows the classification of tires as a function of their hydroplaning sensitivity. $U_x^{(b)}$ quantify the amount of water that is pushed out streamwise, the part that is not evacuated and by-passes the tire at the shoulder or that which is drained into the grooves. We can think that for the same vehicle speed V_0, a tire with higher $U_x^{(b)}$ stocks more water in the water bank and is more sensitive to the hydroplaning mechanisms.

However, the draining effect through the grooves was not investigated in the present paper. The resolution used here is too low to allow the velocity field calculation in the tire grooves. Therefore, velocity measurements inside the grooves remain the most important challenge in order to characterize the flow either in grooves of A, B or C types. The potential presence of multiphase flow or eventually turbulence can be a key factor to understand the draining capacity of a tire as a function of the geometry of its grooves.

Nomenclature

d_p	Seeding particle diameter (m)
g	Gravity acceleration (m.s^{-2})
h_0	Water height of the puddle at rest (m)
n_w	Refractive index of water
n_p	Refractive index of PMMA
PIV	Particle image velocimetry
PMMA	Polymethyl methacrylate
U	Velocity of the fluid (m.s^{-1})
U_x	and U_y Streamwise and spanwise fluid velocities (m.s^{-1})
$U_x^{(b)}$	Spatial averaged streamwise velocity in the water bank (m.s^{-1})
$U_y^{(s)}$	Spatial averaged spanwise velocity at the shoulder (m.s^{-1})
V_0	Vehicle speed (m.s^{-1})
V_p	Falling velocity of seeding particles (m.s^{-1})
z_f	Falling distance of seeding particles (m)
z^*	Normalised ($/h_0$) height of solid particles in the puddle
$< . >$	Ensemble average for any quantity or profile
max.	Maximum of profile
θ_p	Angle of the inclined face of the transparent window (°)
δt	Time step between laser pulses (s)
μ	Water dynamic viscosity (Kg.m.s^2)
ρ	Water density (Kg.m^{-3})
ρ_p	Seeding particle density (m)

The authors would like to thank BPI France (grant n° DOS0051329/00) and Région Auvergne-Rhône-Alpes (grant n° 16 015011 01) for funding the Hydrosafe Tire FUI project.

References

[1] B.J. Allbert, Tires and Hydroplaning, SAE Trans. **680140** 593–603 (1968)
[2] V. Todoroff, S. Paupy, F. Biesse, Y. Le Chenadec, The mechanisms involved during the wet braking of new and worn tires, Veh. Syst. Dyn. **57**, 1–20 (2018)
[3] R.C. Dreher, W.B. Horne, Phenomena of pneumatic tire hydroplaning, Procedia Social Behav. Sci. **53**, 1019–1027 (1963)
[4] W. Gengenbach, Experimental investigation of tires on wet pavements, Auto. Technol. Mag. **70** (1968)
[5] W.B. Horne, T.J. Yager, D.L. Ivey, Recent studies to investigate effects of tire footprint aspect ratio on dynamic hydroplaning speed, The tire pavement interface (1986) ASTM International
[6] A.J. Tuononen, M.J. Matilainen, Real-time estimation of aquaplaning with an optical tyre sensor, Proc. Inst. Mech. Eng. D **223**, 1263–1272 (2009)
[7] A.J. Niskanen, A.J. Tuononen, Three 3-axis accelerometers fixed inside the tyre for studying contact patch deformations in wet conditions, Veh. Syst. Dyn. **52**, 287–298 (2014)
[8] J.R. Cho, H.W. Lee, J.S. Sohn, G.J. Kim, J.S. Woo, Numerical investigation of hydroplaning characteristics of three-dimensional patterned tire, Eur. J. Mech. A/Solids **25**, 914–926 (2006)
[9] C. Hermange, Numerical simulation of the fluid-structure interactions inside the aquaplaning problem. Thèse, Ecole Centrale de Nantes, 2017
[10] S.S. Kumar, K. Anupam, T. Scarpas, C. Kasbergen, Study of hydroplaning risk on rolling and sliding passenger car, Procedia Social Behav. Sci. **53**, 1019–1027 (2012)
[11] S. Vincent, A. Sarthou, J.-P. Caltagirone, F. Sonilhac, P. Février, C. Mignot, G. Pianet, Augmented Lagrangian and penalty methods for the simulation of two-phase flows interacting with moving solids. Application to hydroplaning flows interacting with real tire tread patterns, J. Comput. Phys. **230**, 956–983 (2011)
[12] T. Suzuki, T. Fujikawa, Improvement of hydroplaning performance based on water flow around tires, SAE Technical Paper (2001)
[13] R.J. Adrian, C.-S. Yao, Pulsed laser technique application to liquid and gaseous flows and the scattering power of seed materials, Appl. Opt. **24**, 44–52 (1985)
[14] R.J. Adrian, Particle-imaging techniques for experimental fluid mechanics, Ann. Rev. Fluid Mech. **23**, 261–304 (1991)
[15] R. Kingslake, Optics in photography, SPIE, Washington, 1992.

Cite this article as: D. Cabut, M. Michard, S. Simoens, V. Todoroff, J. Lemaître, C. Hermange, Y. Le Chenadec, Particle Image Velocimetry (PIV) measurements in a water film, application to a tire rolling through a puddle, Mechanics & Industry **20**, 811 (2019)